Editors' Suggestion

Vibrational modes as the origin of dielectric loss at 0.27–100 THz in *a*-SiC:H

B.T. Buijtendorp,[1,*] A. Endo,[1] W. Jellema,[2] K. Karatsu,[3] K. Kouwenhoven,[1,3] D. Lamers,[3] A.J. van der Linden,[3] K. Rostem,[4] H.M. Veen,[3] E.J. Wollack,[4] J.J.A. Baselmans,[1,3,5] and S. Vollebregt[1]

[1] *Faculty of Electrical Engineering, Mathematics and Computer Science, Delft University of Technology, Mekelweg 4, 2628 CD Delft, Netherlands*

[2] *SRON Netherlands Institute for Space Research, Landleven 12, 9747 AD Groningen, Netherlands*

[3] *SRON Netherlands Institute for Space Research, Niels Bohrweg 4, 2333 CA Leiden, Netherlands*

[4] *NASA/Goddard Space Flight Center, Code 665, Greenbelt, Maryland 20771, USA*

[5] *Physikalisches Institut, Universität zu Köln, Zülpicher Straße 77, 50937 Cologne, Germany*

(Received 22 May 2024; accepted 15 November 2024; published 17 January 2025)

Low-loss deposited dielectrics are beneficial for the advancement of superconducting integrated circuits for astronomy. In the microwave band (approximately 1–10 GHz) the dielectric loss at cryogenic temperatures and low electric field strengths is dominated by two-level systems. However, the origin of the loss in the millimeter-submillimeter band (approximately 0.1–1 THz) is not understood. We measured the loss of hydrogenated-amorphous-SiC films in the 0.27–100-THz range using superconducting-microstrip resonators and Fourier-transform spectroscopy. The agreement between the loss data and a Maxwell-Helmholtz-Drude dispersion model suggests that vibrational modes above 10 THz dominate the loss in hydrogenated amorphous SiC above 200 GHz.

DOI: 10.1103/PhysRevApplied.23.014035

I. INTRODUCTION

Deposited dielectrics with low loss at millimeter-submillimeter wavelengths are beneficial for the development of superconducting integrated circuits for astronomy, such as filter banks [1–4], on-chip Fourier-transform spectrometers [5], and kinetic-inductance parametric amplifiers [6]. Although it is possible to fabricate microstrip lines with the use of crystalline Si (*c*-Si) extracted from a silicon-on-insulator wafer by a flip-bonding process [7], deposited dielectrics allow simpler and more-flexible chip designs and fabrication routes. Recently there have been multiple reports of excess loss in deposited dielectrics in the millimeter-submillimeter band (approximately 0.1–1 THz) compared with the microwave band (approximately 1–10 GHz) [8–11], and it was found that the millimeter-submillimeter loss increases monotonically with frequency [8,11]. The frequency dependence of the loss is surprising in the framework of the standard tunneling model for two-level systems (TLSs) [12,13]. Although the standard tunneling model successfully explains the dielectric loss in the microwave band at cryogenic temperatures and low electric field strengths, the origin of the millimeter-submillimeter loss is not understood.

We measured the loss of hydrogenated-amorphous-SiC (*a*-SiC:H) films in the 0.27–100-THz range, where in the 270–600-GHz range we used superconducting-microstrip resonators, and above 3 THz we used Fourier-transform spectroscopy (FTS). The agreement between the loss data and a Maxwell-Helmholtz-Drude (MHD) dispersion model suggests that vibrational modes above 10 THz dominate the loss in *a*-SiC:H above 200 GHz.

II. DEPOSITION DETAILS AND MATERIAL CHARACTERIZATION OF *a*-SiC:H

We deposited the 2.1-μm-thick *a*-SiC:H films by plasma-enhanced chemical vapor deposition using a Novellus Concept One system [14]. All the *a*-SiC:H films that we measured in this work were deposited together on a total of four *c*-Si wafers (W1–W4). We fabricated the microstrip resonators on W1, and on this wafer we deposited *a*-SiC:H on a Nb-Ti-N ground layer that was sputter-deposited on the *c*-Si substrate. On W2–W4 we deposited *a*-SiC:H directly on the *c*-Si substrates. Before the deposition of *a*-SiC:H we removed any native oxide on each wafer with a 10-s 10%-HF dip. We deposited the

*Contact author: b.t.buijtendorp@tudelft.nl

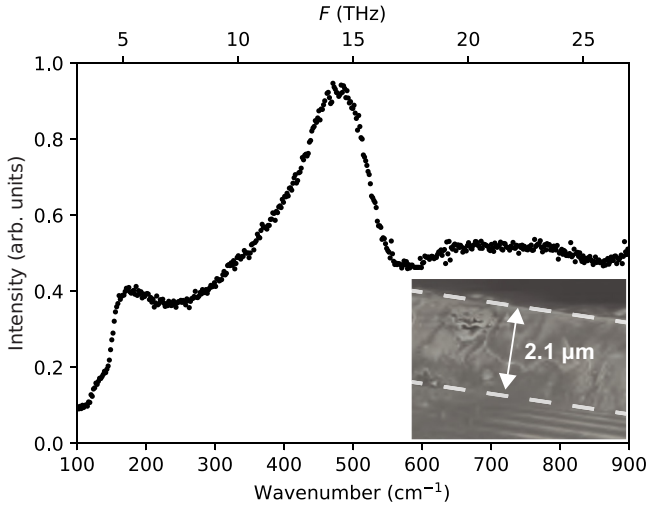

FIG. 1. Raman spectrum of a 2.1-μm-thick *a*-SiC:H film on a *c*-Si substrate. The Raman spectrum is typical of fully amorphous SiC:H. The inset shows a scanning electron micrograph of a cleaved *c*-Si wafer with an *a*-SiC:H film, from which we determined the film thickness.

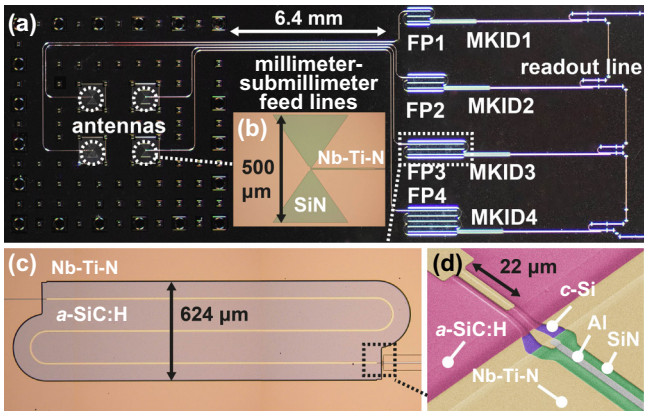

FIG. 2. (a) Photograph of the loss-measurement device. The FP resonators receive the millimeter-submillimeter signal from antennas, which receive radiation from a Toptica Photonics TeraScan 780 photomixer source. Each FP resonator is coupled to an MKID, which detects the power transmitted through the FP resonator. (b) Micrograph of one of the leaky-wave antennas. (c) Micrograph of FP resonator 3 (FP3). The feed line is visible on the left side of the image and the MKID is visible on the right side of the image. (d) Tilted scanning electron micrograph of the coupling of FP3 to the MKID, with false coloring.

films at a substrate temperature of 400 °C, a SiH_4 flow of 25 sccm, a CH_4 flow of 411 sccm, a chamber pressure of 2 Torr, 450-kHz rf power of 150 W, and 13.56-MHz rf power of 450 W.

We performed several characterization measurements on W2 to determine the material properties of the *a*-SiC:H films. We verified that the SiC:H is fully amorphous by performing Raman spectroscopy with a 514-nm laser. We plot the Raman spectrum in Fig. 1. The spectrum's broadened features are typical of fully amorphous SiC:H [15–17]. We determined that the *a*-SiC:H has an atomic Si:C ratio of 0.8 using energy-dispersive x-ray spectroscopy. We measured a 2.1-μm film thickness from a scanning electron micrograph of the cross section of the wafer, as shown in the inset in Fig. 1. Finally, we measured a relative dielectric constant ε_r' of 7.6 at 250 THz and a band gap of 1.8 eV by performing ellipsometry and fitting a Tauc-Lorentz dispersion model [18].

III. FAR-INFRARED LOSS, MEASURED IN SUPERCONDUCTING-MICROSTRIP RESONATORS

A. Device design and fabrication

To measure the 270–600-GHz loss of *a*-SiC:H we used a lab-on-a-chip experiment based on superconducting Fabry-Pérot (FP) resonators fabricated from *a*-SiC:H and Nb-Ti-N. The design of the loss-measurement device [Fig. 2(a)] is similar to the one reported in Refs. [8,9], with the exception that we enabled wideband measurements by using leaky-wave antennas [Fig. 2(b)] fabricated on 1-μm-thick SiN_x membranes [19,20]. The signal from each antenna is coupled to an FP resonator via a Nb-Ti-N coplanar waveguide (CPW) with 2-μm center-line width and 2-μm gap width, designed to eliminate radiation loss [21]. The four FP resonators have a Nb-Ti-N/*a*-SiC:H/Nb-Ti-N microstrip geometry with 2.1-μm-thick *a*-SiC:H and 14-μm line width. The power transmitted through the FP resonators is measured with CPW (Nb-Ti-N)-Al hybrid microwave kinetic-inductance detectors (MKIDs) [22]. The couplings between the FP resonators and the input and output CPW lines are made at the ends of each FP resonator, with a 22-μm-long overlap between the FP microstrip lines and the center lines of the Nb-Ti-N CPWs [Fig. 2(d)]. The galvanic connections between the Nb-Ti-N center lines, which are coupled to the FP resonators and the Al center lines of the CPW (Nb-Ti-N)-Al hybrid MKIDs, are made on a layer of SiN_x [Fig. 2(d)] to avoid enhanced erosion of the Al at the Si/Nb-Ti-N interfaces [23].

We optimized the FP-resonator and FP-coupler design to cover the wide bandwidth of 270–600 GHz. We limited the maximum value of the FP resonators' coupling quality factor Q_c such that (1) the FP peaks do not become too sharp to measure with the 20-MHz resolution of the photomixer source that generates the 270–600-GHz radiation and (2) there is sufficient transmission at higher frequencies where the losses are high. Furthermore, we limited the minimum value of Q_c so that the FP transmission peaks do not have too much overlap to be individually resolved. Taking these limitations into consideration, we chose resonator lengths of 3.00, 4.50, 6.75, and 10.13 mm and a coupler overlap length of 22 μm [Fig. 2(d)], resulting in

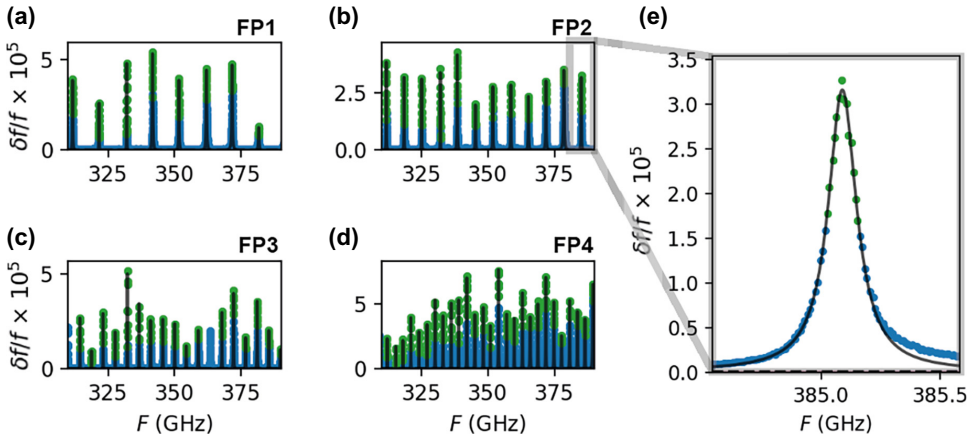

FIG. 3. (a)–(d) Measured MKID frequency response of FP resonators 1–4 (FP1–FP4) in the 310–380-GHz band. The blue and green points represent the measurement data. The data represented as green points were used in the fitting. The black curves are Lorentzian fits to the FP-resonator transmission peaks, from which we obtained the loaded quality factor Q of each FP-resonator peak. The same analysis was performed for each of the seven frequency bands centered at 270, 310, 350, 400, 455, 520, and 600 GHz. (e) Close-up of a single transmission peak of FP2.

Q_c values in ranging from 0.4×10^3 to 24×10^3 in the 600–270-GHz range for all four FP resonators.

We fabricated the device on a high-resistivity c-Si wafer (W1). We coated the wafer with 1 μm of SiN_x on the front side and on the back side, using low-pressure chemical vapor deposition. We removed the SiN_x front side everywhere except at the antennas and at the Al lines of the MKIDs. We sputter-deposited the 300-nm-thick Nb-Ti-N ground layer (under the a-SiC:H), the 100-nm thick Nb-Ti-N top layer (on top of the a-SiC:H), and the 100-nm thick Al layer using an Evatec LLS 801 system. We deposited the a-SiC:H on top of the Nb-Ti-N ground layer, as discussed in Sec. II. We etched the a-SiC:H using reactive-ion etching (RIE) with an SF_6 and O_2 plasma. We patterned the leaky-wave antennas, CPW millimeter-submillimeter feed lines, MKIDs, and CPW microwave readout lines into the Nb-Ti-N ground plane using RIE. We wet-etched the Al center lines of the MKIDs. We patterned the SiN_x on the back side using RIE to define KOH-etching windows behind the four antennas, and we removed the c-Si substrate below the antennas by KOH etching, such that each antenna sits on top of a SiN_x membrane. Subsequently, for stray-light absorption, we covered the back side of the chip with a β-Ta mesh [24], which we sputter-deposited using the Evatec LLS 801 system. We removed the β-Ta below the SiN_x membranes using RIE.

B. Measurement

We measured the loss at 20 mK on the chip that is described in Sec. III A and shown in Fig. 2(a). The experimental setup was similar to the one reported in Refs. [8,9]. The radiation from a continous-wave photomixer source (Toptica Photonics Terascan 780) was swept from 270 to 600 GHz in frequency steps of 20 MHz. The broad beam from the photomixer source was weakly coupled to all four antennas. The loss of the a-SiC:H was determined from the power that was transmitted through the FP resonators, measured by the response of the MKIDs as a function of frequency. The transmitted power versus frequency is a sum of Lorentzian peaks located at $f_{\text{peak}} = nf_0$, where n is the mode number and f_0 is the fundamental resonance frequency. In Figs. 3(a)–3(d) we plot the measured MKID response in a frequency band around 350 GHz. Each peak corresponds to a loaded quality factor $Q = f_{\text{peak}}/\Delta f$, where Δf is the peak's full width at half maximum.

C. Results

We determined the 270–600-GHz loss by fitting Lorentzian peaks to the MKID response data. We plot the measured MKID response in the 310–380-GHz frequency band in Fig. 3. The variation in the peak heights in Fig. 3 is caused by a variation in the millimeter-submillimeter power that enters the FP resonators, due to a frequency dependence of the power output of the photomixer source and due to standing waves between the antennas and the FP resonators. We determined the Q value of each peak from a Lorentzian fit [Fig. 3(e)], where the fitting parameter Q is independent of the peak height. For the next steps in the analysis, we separated the frequency response data into frequency bands centered at 270, 310, 350, 400, 455, 520, and 600 GHz. We determined the Q and n values at the center frequencies of each band from the average values computed over all peaks within each band. We present the average-Q-versus-average-n data in Fig. 4.

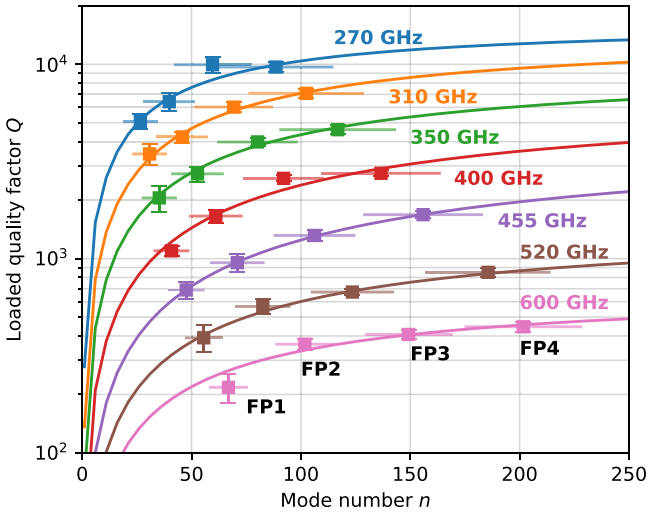

FIG. 4. Average loaded quality factor Q versus average mode number n of the Fabry-Pérot resonators (FP1–FP4). The curves are fits of Eq. (1). The vertical error bars represent the standard deviation ($\pm\sigma$) in Q. The horizontal bars represent the range of mode numbers used in our computing the average.

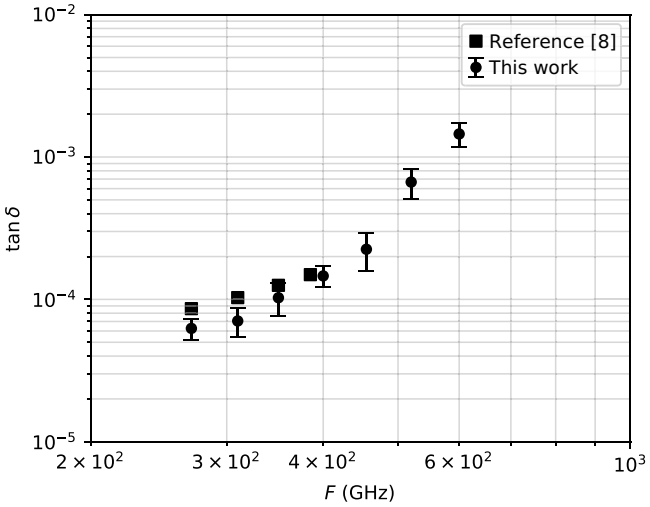

FIG. 5. The millimeter-submillimeter $\tan\delta = 1/pQ_i$ versus frequency, which we obtained by fitting Eq. (1) to the data in Fig. 4. The points represent the measured $\tan\delta$ values from this work, and the error bars represent 1 standard deviation ($\pm\sigma$) uncertainty in $\tan\delta$. The squares show the a-SiC:H losses reported in Ref. [8].

We determined the internal quality factor Q_i from the Q-versus-n data by fitting the equation

$$Q = \frac{nQ_{c,1}Q_i}{nQ_{c,1} + Q_i}, \tag{1}$$

where $Q_c = nQ_{c,1}$ is the FP resonator's coupling quality factor. Here, $Q_{c,1} = \pi/|t_c|^2$, where t_c is the transmission coefficient of the FP resonators' couplers. The FP resonators have identical couplers and therefore share a single $Q_{c,1}$ (and hence t_c) value, which is obtained together with Q_i from the fit (Fig. 4) of Eq. (1). Finally, from the FP resonators' internal quality factor Q_i we obtained the loss tangent $\tan\delta$:

$$\tan\delta = (pQ_i)^{-1}, \tag{2}$$

where p is the filling fraction of the a-SiC:H, which we determined to be 0.97 in our FP resonators using the electromagnetic field solver SONNET [25]. We present the resulting loss-versus-frequency data in the 270–600-GHz range in Fig. 5. We observe that the loss increases monotonically with frequency and that it is in agreement with the loss reported in Ref. [8].

IV. MID-INFRARED LOSS MEASURED BY FOURIER-TRANSFORM SPECTROSCOPY

A. Sample fabrication

To measure the 3–100-THz loss of the a-SiC:H we fabricated three kinds of a-SiC:H samples for FTS measurements. Sample 1 (S1) is a single a-SiC:H membrane with 2.1 μm thickness and 2×2 cm^2 surface area, supported by a 400-μm-thick c-Si frame. Sample 2 (S2) is a stack of two units that are equivalent to S1, as shown in Fig. 6(b). Sample 3 (S3) is a 2.1-μm-thick a-SiC:H film (not a membrane) on a double-side-polished c-Si substrate. We fabricated S1 and S2 from W3 and fabricated S3 from W4. The a-SiC:H films that were fabricated into membranes were deposited on the front side of the substrates, and were deposited simultaneously with the other a-SiC:H samples that are described in this work. Separately, we deposited an a-SiC:H layer on the back side of W3. This back-side layer was removed by RIE below the membrane positions, thereby creating square etching windows. The membranes were then created by our removing the c-Si substrate from the back side of the wafer using KOH etching.

B. Measurement

To obtain the 3–100-THz loss, we measured the FTS transmission of S1–S3 at room temperature. The FTS transmission is defined as $T \equiv I_s/I_{BG}$. I_s is the measured intensity when the sample is in the path from the source to the detector [Fig. 6(a)], and I_{BG} is the measured intensity without a sample in place. We measured the transmission through S1 and S2 in the 3–10-THz and 18–30-THz ranges using a BioRad FTS system, at a resolution of 2.0 cm^{-1} for S1 and 0.5 cm^{-1} for S2. In Fig. 6(a) we present a photograph of S2 inside the BioRad FTS system. We used a room-temperature deuterated triglycine sulfate detector for frequencies above 4 THz and a cryogenic bolometer detector for frequencies below 4 THz. The sample chamber

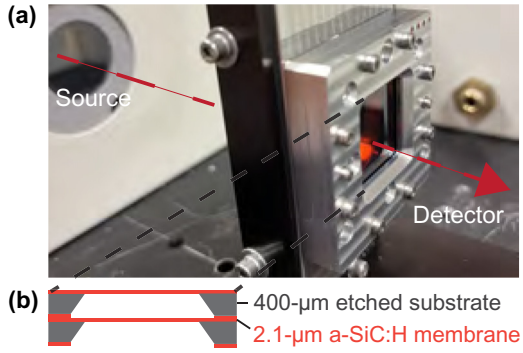

FIG. 6. (a) Photograph of S2 in the BioRad FTS system. (b) Schematic of S2, which consists of two stacked *a*-SiC:H membranes.

of the BioRad FTS system was continuously purged with dry air before and during the measurement. Furthermore, we measured the transmission through S3 in the 18–100-THz range using a Thermo Fischer Nicolet FTS system at a resolution of 4.0 cm^{-1}, where the sample chamber was continuously purged with nitrogen before and during the measurement.

C. Results

We determined the 3–100-THz loss by fitting transfer-matrix-method (TMM) [26] models to the FTS transmission data for S1–S3. The transmission data and the best-fit transmission curves are presented in Fig. 7(a). Here the complex permittivity $\hat{\varepsilon}_r \equiv \varepsilon_r' + i\varepsilon_r''$ (and therefore the loss) of *a*-SiC:H was a model parameter that we obtained from the fitting. We combined the FTS transmission data for S1–S3 in a single fitting procedure, where we normalized the fitting residuals by the number of data points in each dataset. In the case of S3, we measured the bare *c*-Si substrate before the deposition of *a*-SiC:H and we included the substrate properties in the TMM model. We note that the periodicity in the transmission of S2 [Fig. 7(a)] is dictated by the intermembrane distance.

In the fitting of the TMM models to the transmission data we parameterized $\hat{\varepsilon}_r$ of *a*-SiC:H using the MHD dispersion model [27,28]:

$$\hat{\varepsilon}_r = \hat{\varepsilon}_\infty + \sum_{j=1}^{M} \frac{\Delta\hat{\varepsilon}_j \omega_{T_j}^2}{\omega_{T_j}^2 - \omega^2 - i\omega\Gamma_j'(\omega)}, \tag{3}$$

where $\hat{\varepsilon}_r$ consists of a sum of M modes. The broadening Γ_j' is given by

$$\Gamma_j' = \Gamma_j \exp\left[-\alpha_j \left(\frac{\omega_{T_j}^2 - \omega^2}{\omega\Gamma_j}\right)^2\right], \tag{4}$$

where the broadening is purely Lorentzian if α_j equals zero, and is an interpolation between Lorentzian and Gaussian if α_j is greater than zero [27,29]. Γ_j is the Lorentzian damping coefficient, ω_{T_j} is the center frequency of a mode, and $\Delta\hat{\varepsilon}_j$ is defined as $\Delta\hat{\varepsilon}_j \equiv \hat{\varepsilon}_j - \hat{\varepsilon}_{j+1}$. The modes are ordered such that $\omega_{T_{j+1}} > \omega_{T_j}$. $\hat{\varepsilon}_\infty \equiv \hat{\varepsilon}_{M+1}$ is the contribution from modes at higher frequencies.

In Fig. 7(b) we present $\hat{\varepsilon}_r$ of *a*-SiC:H resulting from the best-fit parameters, which are listed in Table I in

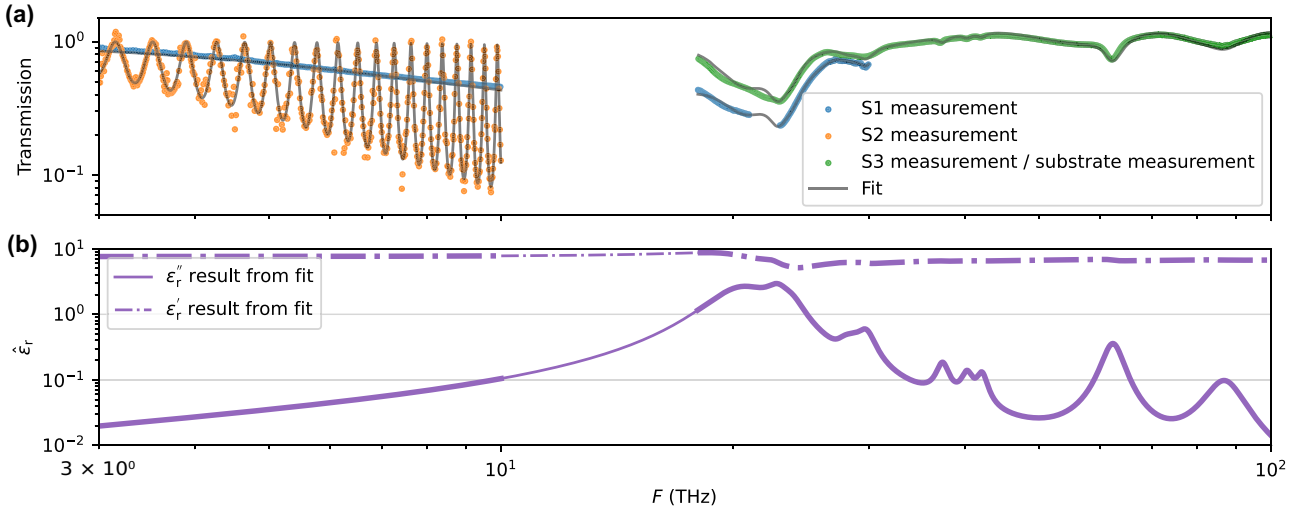

FIG. 7. (a) Transmission (points) through the *a*-SiC:H samples measured by FTS in the 3–100-THz range for S1–S3. The solid gray curves show the best-fit results of TMM models where $\hat{\varepsilon}_r$ is parameterized with the MHD dispersion model [Eq. (3)]. The plotted data for S3 were divided by the measured transmission of the bare *c*-Si substrate to clearly show the absorption features of the *a*-SiC:H. (b) The real (ε_r') and imaginary (ε_r'') parts of the complex permittivity $\hat{\varepsilon}_r$ resulting from the fitting to the transmission data in Fig. 7(a). The thin curves show the fitting results in the 3–100-THz range, and the thick curves show the ranges where measurement data were available. The annotations identify the modes that are present in the absorption spectrum, which are detailed in the Appendix.

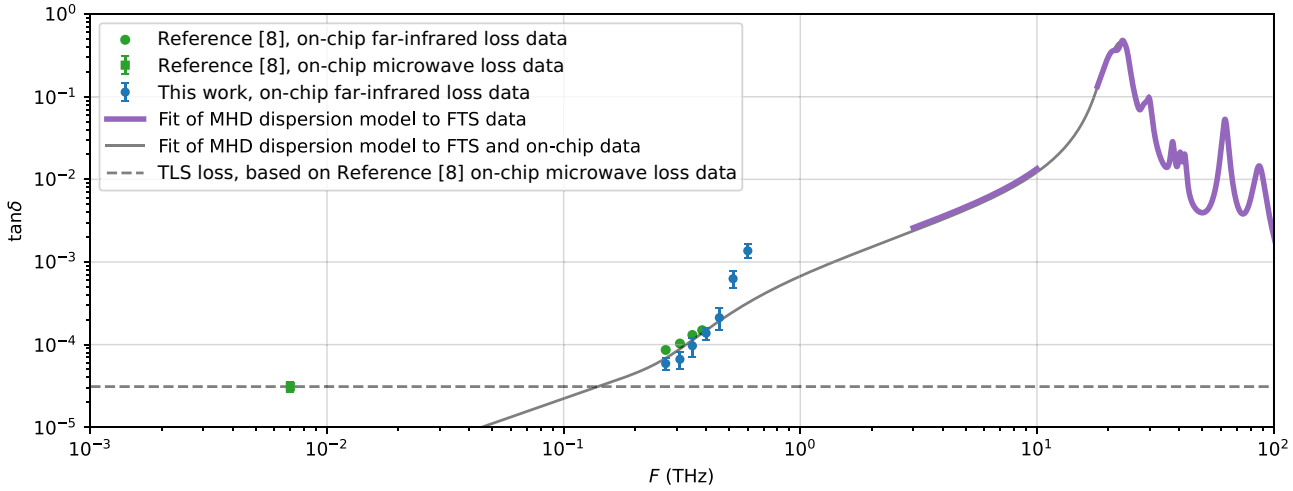

FIG. 8. Loss tangent $\tan\delta$ versus frequency for *a*-SiC:H. The solid gray curve represents the $\tan\delta$ that we obtained by fitting the MHD dispersion model to the combined FTS-measured transmission data [Fig. 7(a)] and FP resonator–measured loss data (Fig. 5), as described in Sec. V. The purple curve represents the $\tan\delta$ that we obtained by fitting the MHD dispersion model [Eq. (3)] to only the FTS data [Fig. 7(a)]. The blue points represent the FP resonator–measured loss data from this work (Fig. 5). The green points represent the *a*-SiC:H loss data reported in Ref. [8]. The intersection of the solid gray curve and the horizontal dashed line illustrates the crossover between the low-power cryogenic TLS loss and the loss due to vibrational modes.

the Appendix. The observed vibrational modes were reported previously in the literature [30]: the Si—C-stretch absorption band (approximately 18–30 THz), the Si—CH_2—Si wagging mode (approximately 30–31 THz), the Si—CH_2—Si scissor and bending modes (approximately 40 THz), the C—H_3 symmetric (approximately 37 THz) and asymmetric (approximately 42 THz) bending bands, the Si—H_x-stretch band (approximately 60–69 THz), and the C—H_x-stretch band (approximately 84–93 THz). The purple curve in Fig. 8 represents $\tan\delta = \varepsilon_r''/\varepsilon_r'$, corresponding to $\hat{\varepsilon}_r$ (purple curve) plotted in Fig. 7(b).

V. MODEL OF DIELECTRIC LOSS FROM MICROWAVE TO MID-INFRARED WAVELENGTHS

Finally, we examined whether the loss measured with the FP resonators at 270–600 GHz and at 20 mK (Fig. 5) and the loss measured by FTS in the 3–100-THz range and at room temperature [Fig. 7(b)] can be consistently explained with a common MHD dispersion model. Here we note that amorphous dielectrics typically exhibit negligible temperature dependence of the dielectric loss at infrared wavelengths [31]. We searched for a set of parameters in Eq. (3) using a numerical optimization algorithm that simultaneously minimizes the differences between (1) the calculated $\tan\delta$ and the FP resonator–measured $\tan\delta$ and (2) the calculated transmission and the FTS-measured transmission. In the fitting we included the FP resonator–measured $\tan\delta$ values from Ref. [8] (Fig. 5). The 520- and 600-GHz points in Fig. 5 had to be excluded because they could not be reproduced by our current model. The resulting best-fit parameter values are listed in Table II in the Appendix. In Fig. 8 we plot $\tan\delta$ resulting from the combined fitting to the FTS and FP-resonator measurements (gray curve), and $\tan\delta$ corresponding to Fig. 7(b) resulting from FTS measurements alone (purple curve). Except for the points at 520 and 600 GHz (which are discussed in the next section), the modeled frequency dependence of $\tan\delta$ agrees well with both the FP-resonator measurements and the FTS measurements over the entire frequency range that was covered.

VI. DISCUSSION OF THE ORIGIN OF THE LOSS IN DEPOSITED DIELECTRICS

Our results show that the absorption tail of vibrational modes located at frequencies above 10 THz can explain the measured losses in the 270–455-GHz range. Above a frequency of roughly 200 GHz the losses are anticipated to be dominated by vibrational modes, and below a frequency of roughly 200 GHz and at cryogenic temperatures and low power the loss is expected to be dominated by TLSs. At 520 and 600 GHz the on-chip loss data are not reproducible by the MHD dispersion model with the modes that have been reported in the literature. For an overview of the modes in amorphous and crystalline SiC, see Refs. [30,32]. The excess loss at 520 and 600 GHz is not expected to originate from the bulk of the superconductor since the Nb-Ti-N has an energy gap of roughly 1.1 THz. However, it is possible that the excess loss is caused by a small fraction of the superconductor that behaves differently from the

bulk of the superconductor [33–35]. More experiments are needed to clarify this discrepancy between the model and our data at 520 and 600 GHz.

Our results pave the way for a thorough understanding of the dielectric loss in deposited dielectrics from microwave to near-infrared wavelengths. We emphasize that strong vibrational modes in the 10–30-THz range are present not only in *a*-SiC:H but have also been reported for other commonly used deposited dielectrics, such as *a*-Si:H [36,37], SiN_x [27], and SiO_x [28]. Furthermore, the TLS loss-tangent values at cryogenic temperatures and low electric field strengths reported at microwave frequencies of *a*-Si:H (approximately 10^{-5}) [9,10,38], SiN_x (approximately 10^{-4}) [10], and SiO_x (approximately 10^{-4}–10^{-3}) [10,39] lead us to anticipate a similar crossover for these materials from loss dominated by TLSs to loss dominated by vibrational modes.

VII. CONCLUSION

We demonstrated that the dielectric loss of *a*-SiC:H above 200 GHz is dominated by the absorption tail of vibrational modes that are located at frequencies above 10 THz. Our results pave the way for a thorough understanding of the dielectric loss in deposited dielectrics from microwave to near-infrared wavelengths.

ACKNOWLEDGMENTS

We thank the staff of the Else Kooi Laboratory and the Kavli Nanolab Delft for their support. This work was supported by the European Union (European Research Council Consolidator Grant No. 101043486 TIFUUN). J.J.A.B. acknowledges support through the Global Faculty Program of the University of Cologne.

The views and opinions expressed are those of the authors only and do not necessarily reflect those of the European Union or the European Research Council Executive Agency. Neither the European Union nor the granting authority can be held responsible for them.

APPENDIX: FTS FITTING PARAMETERS

In this appendix we provide the best-fit values of the FTS fitting parameters corresponding to Figs. 7 and 8.

TABLE I. Best-fit values corresponding to the results in Fig. 7(b) of the MHD-dispersion-model parameters [Eq. (3)]. The MHD dispersion model was fitted to only the FTS-measured transmission data [Fig. 7(a)]. ε_∞ resulting from the fit is 6.8. The values shown in bold were constrained to the listed values to reduce the number of free fitting parameters.

j	Vibrational mode	$\omega_{Tj}/2\pi$ (THz)	$\Delta\varepsilon'_j$	Γ_j (THz)	α_j
1	Si—C stretch	20.7	5.5×10^{-1}	4.6	**0**
2	Si—C stretch	22.8	9.8×10^{-2}	1.7	3.8×10^{-2}
3	Si—C stretch	23.9	5.8×10^{-2}	1.9	**0**
4	Si—CH_2—Si wag	28.3	9.0×10^{-3}	1.7	4.2×10^{-1}
5	Si—CH_2—Si wag	29.8	2.5×10^{-2}	1.8	**0**
6	C—H_3 symmetric bend	37.4	$\mathbf{5.0 \times 10^{-3}}$	**1.5**	2.6×10^{-6}
7	Si—CH_2—Si scissor or symmetric bend	40.3	$\mathbf{3.0 \times 10^{-3}}$	**1.5**	**0**
8	C—H_3 asymmetric bend	42.1	$\mathbf{3.0 \times 10^{-3}}$	**1.5**	**0**
9	Si–H_x stretch	62.3	2.2×10^{-2}	**4.0**	**0**
10	C—H_x stretch	**87.0**	1.1×10^{-2}	**10.0**	**0**

TABLE II. Best-fit values corresponding to the solid gray curve in Fig. 8 of the MHD-dispersion-model parameters [Eq. (3)]. The MHD dispersion model was fitted to the combined FTS-measured transmission data [Fig. 7(a)] and the FP resonator–measured loss data (Fig. 5). ε_∞ resulting from the fit is 6.8. The values shown in bold were constrained to the listed values to reduce the number of free fitting parameters.

j	Vibrational mode	$\omega_{Tj}/2\pi$ (THz)	$\Delta\varepsilon'_j$	Γ_j (THz)	α_j
1	Si—C stretch	19.6	1.9×10^{-1}	3.1	**0**
2	Si—C stretch	22.1	4.8×10^{-1}	4.2	1.5×10^{-5}
3	Si—C stretch	23.5	3.3×10^{-2}	1.2	**0**
4	Si—CH_2—Si wag	28.5	9.3×10^{-3}	1.5	5.2×10^{-1}
5	Si—CH_2—Si wag	29.8	1.6×10^{-2}	1.2	**0**
6	C—H_3 symmetric bend	37.4	$\mathbf{5.0 \times 10^{-3}}$	**1.5**	6.2×10^{-7}
7	Si—CH_2—Si scissor or symmetric bend	40.2	$\mathbf{3.0 \times 10^{-3}}$	**1.5**	**0**
8	C—H_3 asymmetric bend	42.1	$\mathbf{3.0 \times 10^{-3}}$	**1.5**	**0**
9	Si—H_x stretch	62.3	2.3×10^{-2}	**4.0**	**0**
10	C—H_x stretch	**87.0**	1.1×10^{-2}	**10.0**	**0**

[1] A. Taniguchi *et al.*, DESHIMA 2.0: Development of an integrated superconducting spectrometer for science-grade astronomical observations, J. Low Temp. Phys. **209**, 278 (2022).

[2] A. Pascual Laguna, K. Karatsu, D. Thoen, V. Murugesan, B. Buijtendorp, A. Endo, and J. Baselmans, Terahertz bandpass filters for wideband superconducting on-chip filterbank spectrometers, IEEE Trans. Terahertz Sci. Technol. **11**, 635 (2021).

[3] K. S. Karkare, P. S. Barry, C. M. Bradford, S. Chapman, S. Doyle, J. Glenn, S. Gordon, S. Hailey-Dunsheath, R. M. J. Janssen, A. Kovács, H. G. LeDuc, P. Mauskopf, R. McGeehan, J. Redford, E. Shirokoff, C. Tucker, J. Wheeler, and J. Zmuidzinas, Full-array noise performance of deployment-grade SuperSpec mm-wave on-chip spectrometers, J. Low Temp. Phys. **199**, 849 (2020).

[4] S. Hailey-Dunsheath *et al.*, Optical measurements of SuperSpec: A millimeter-wave on-chip spectrometer, J. Low Temp. Phys. **176**, 841 (2014).

[5] R. Basu Thakur, A. Steiger, S. Shu, F. Faramarzi, N. Klimovich, P. K. Day, E. Shirokoff, P. D. Mauskopf, and P. S. Barry, Development of superconducting on-chip Fourier transform spectrometers, J. Low Temp. Phys. **211**, 227 (2023).

[6] B.-K. Tan, N. Klimovich, R. Stephenson, F. Faramarzi, and P. Day, Operation of kinetic-inductance travelling wave parametric amplifiers at millimetre wavelengths, Supercond. Sci. Technol. **37**, 035006 (2024).

[7] A. Patel, A. Brown, W. Hsieh, T. Stevenson, S. H. Moseley, K. U-yen, N. Ehsan, E. Barrentine, G. Manos, and E. J. Wollack, Fabrication of MKIDS for the MicroSpec spectrometer, IEEE Trans. Appl. Supercond. **23**, 2400404 (2013).

[8] B. Buijtendorp, S. Vollebregt, K. Karatsu, D. Thoen, V. Murugesan, K. Kouwenhoven, S. Hähnle, J. Baselmans, and A. Endo, Hydrogenated amorphous silicon carbide: A low-loss deposited dielectric for microwave to submillimeter-wave superconducting circuits, Phys. Rev. Appl. **18**, 064003 (2022).

[9] S. Hähnle, K. Kouwenhoven, B. Buijtendorp, A. Endo, K. Karatsu, D. Thoen, V. Murugesan, and J. Baselmans, Superconducting microstrip losses at microwave and submillimeter wavelengths, Phys. Rev. Appl. **16**, 014019 (2021).

[10] A. D. O'Connell, M. Ansmann, R. C. Bialczak, M. Hofheinz, N. Katz, E. Lucero, C. McKenney, M. Neeley, H. Wang, E. M. Weig, A. N. Cleland, and J. M. Martinis, Microwave dielectric loss at single photon energies and millikelvin temperatures, Appl. Phys. Lett. **92**, 112903 (2008).

[11] A. Endo, C. Sfiligoj, S. J. C. Yates, J. J. A. Baselmans, D. J. Thoen, S. M. H. Javadzadeh, P. P. van der Werf, A. M. Baryshev, and T. M. Klapwijk, On-chip filter bank spectroscopy at 600–700 GHz using NbTiN superconducting resonators, Appl. Phys. Lett. **103**, 032601 (2013).

[12] C. Müller, J. H. Cole, and J. Lisenfeld, Towards understanding two-level-systems in amorphous solids: Insights from quantum circuits, Rep. Prog. Phys. **82**, 124501 (2019).

[13] W. A. Phillips, Tunneling states in amorphous solids, J. Low Temp. Phys. **7**, 351 (1972).

[14] P. Sarro, C. de Boer, E. Korkmaz, and J. Laros, Low-stress PECVD SiC thin films for IC-compatible microstructures, Sens. Actuator A Phys. **67**, 175 (1998).

[15] C. Ricciardi, A. Primiceli, G. Germani, A. Rusconi, and F. Giorgis, Microstructure analysis of a-SiC:H thin films grown by high-growth-rate PECVD, J. Non Cryst. Solids **352**, 1380 (2006).

[16] W. Yu, W. Lu, L. Han, and G. Fu, Structural and optical properties of hydrogenated amorphous silicon carbide films by helicon wave plasma-enhanced chemical vapour deposition, J. Phys. D: Appl. Phys. **37**, 3304 (2004).

[17] S. Nakashima and H. Harima, Raman investigation of SiC polytypes, Phys. Status Solidi (a) **162**, 39 (1997).

[18] J. Budai, I. Hanyecz, E. Szilágyi, and Z. Tóth, Ellipsometric study of Si_xC films: Analysis of Tauc–Lorentz and Gaussian oscillator models, Thin Solid Films **519**, 2985 (2011).

[19] S. Hahnle, O. Yurduseven, S. Van Berkel, N. Llombart, J. Bueno, S. J. C. Yates, V. Murugesan, D. J. Thoen, A. Neto, and J. J. A. Baselmans, An ultrawideband leaky lens antenna for broadband spectroscopic imaging applications, IEEE Trans. Antennas Propag. **68**, 5675 (2020).

[20] A. Neto, UWB, non dispersive radiation from the planarly fed leaky lens antenna—Part 1: Theory and design, IEEE Trans. Antennas Propag. **58**, 2238 (2010).

[21] S. Hähnle, N. V. Marrewijk, A. Endo, K. Karatsu, D. J. Thoen, V. Murugesan, and J. J. A. Baselmans, Suppression of radiation loss in high kinetic inductance superconducting co-planar waveguides, Appl. Phys. Lett. **116**, 182601 (2020).

[22] R. M. J. Janssen, J. J. A. Baselmans, A. Endo, L. Ferrari, S. J. C. Yates, A. M. Baryshev, and T. M. Klapwijk, High optical efficiency and photon noise limited sensitivity of microwave kinetic inductance detectors using phase readout, Appl. Phys. Lett. **103**, 203503 (2013).

[23] L. Ferrari, O. Yurduseven, N. Llombart, S. J. C. Yates, J. Bueno, V. Murugesan, D. J. Thoen, A. Endo, A. M. Baryshev, and J. J. A. Baselmans, Antenna coupled MKID performance verification at 850 GHz for large format astrophysics arrays, IEEE Trans. Terahertz Sci. Technol. **8**, 127 (2018).

[24] J. J. A. Baselmans, S. J. C. Yates, S. M. Doyle, A. Baryshev, J. Bueno, L. Ferrari, N. Llombart, V. Murugesan, D. J. Thoen, O. Yurduseven, and P. Barry, in *Millimeter, Submillimeter, and Far-Infrared Detectors and Instrumentation for Astronomy IX*, edited by J. Zmuidzinas and J.-R. Gao (SPIE, Austin, United States, 2018), p. 67.

[25] Sonnet User's Guide — Sonnet 17.

[26] A. Luce, A. Mahdavi, F. Marquardt, and H. Wankerl, TMM-Fast, a transfer matrix computation package for multilayer thin-film optimization: Tutorial, J. Opt. Soc. Am. A **39**, 1007 (2022).

[27] G. Cataldo, J. A. Beall, H.-M. Cho, B. McAndrew, M. D. Niemack, and E. J. Wollack, Infrared dielectric properties of low-stress silicon nitride, Opt. Lett. **37**, 4200 (2012).

[28] G. Cataldo, E. J. Wollack, A. D. Brown, and K. H. Miller, Infrared dielectric properties of low-stress silicon oxide, Opt. Lett. **41**, 1364 (2016).

[29] C. C. Kim, J. W. Garland, H. Abad, and P. M. Raccah, Modeling the optical dielectric function of semiconductors:

Extension of the critical-point parabolic-band approximation, Phys. Rev. B **45**, 11749 (1992).

[30] S. King, M. French, J. Bielefeld, and W. Lanford, Fourier transform infrared spectroscopy investigation of chemical bonding in low-k a-SiC:H thin films, J. Non Cryst. Solids **357**, 2970 (2011).

[31] U. Strom and P. C. Taylor, Temperature and frequency dependences of the far-infrared and microwave optical absorption in amorphous materials, Phys. Rev. B **16**, 5512 (1977).

[32] A. M. Hofmeister, K. M. Pitman, A. F. Goncharov, and A. K. Speck, Optical constants of silicon carbide for astrophysical applications. II. Extending optical functions from infrared to ultraviolet using single-crystal absorption spectra, Astrophys. J. **696**, 1502 (2009).

[33] V. Lacquaniti, S. Maggi, E. Monticone, and R. Steni, Thickness dependence of electrical and structural properties of Nb thin films, Phys. Status Solidi (a) **151**, 335 (1995).

[34] M. S. M. Minhaj, S. Meepagala, J. T. Chen, and L. E. Wenger, Thickness dependence on the superconducting properties of thin Nb films, Phys. Rev. B **49**, 15235 (1994).

[35] A. Chandrasekaran, R. W. Van De Kruijs, J. M. Sturm, and F. Bijkerk, Nb texture evolution and interdiffusion in Nb/Si-Layered Systems, ACS Appl. Mater. Interfaces **13**, 31260 (2021).

[36] A. A. Langford, M. L. Fleet, B. P. Nelson, W. A. Lanford, and N. Maley, Infrared absorption strength and hydrogen content of hydrogenated amorphous silicon, Phys. Rev. B **45**, 13367 (1992).

[37] B. T. Buijtendorp, J. Bueno, D. J. Thoen, V. Murugesan, P. M. Sberna, J. J. A. Baselmans, S. Vollebregt, and A. Endo, Characterization of low-loss hydrogenated amorphous silicon films for superconducting resonators, J. Astron. Telesc. Instrum. Syst. **8**, 028006 (2022).

[38] B. A. Mazin, D. Sank, S. McHugh, E. A. Lucero, A. Merrill, J. Gao, D. Pappas, D. Moore, and J. Zmuidzinas, Thin film dielectric microstrip kinetic inductance detectors, Appl. Phys. Lett. **96**, 102504 (2010).

[39] J. Gao, A. Vayonakis, O. Noroozian, J. Zmuidzinas, P. K. Day, H. G. Leduc, B. Young, B. Cabrera, and A. Miller, in *The Thirteenth International Workshop on Low Temperature Detectors — LTD13* (Stanford (California), 2009), p. 164.